10. Physisorbed Rare Gas Adlayers Studied with Helium Scattering

G. Comsa, K. Kern, B. Poelsema

Rare gas films physisorbed on single crystal surfaces provide an experimental realization of quasi two-dimensional systems. Due to the competing adsorbate–adsorbate and adsorbate–substrate interactions these systems exhibit an amazingly large number of interesting and quite subtle phenomena, such as commensurate–incommensurate transitions, continuous melting or orientational epitaxy. Going from 2D to 3D, i.e. growing thicker films, epitaxial growth and wetting phenomena can be studied.

Thermal energy helium scattering appears to be particularly appropriate to investigate the properties of these layers. Being a rare gas at thermal energy it is nondestructive and is sensitive to the outermost surface layer; the He wavelength (1–0.5 Å) is well suited for diffraction and its energy (10–100 meV) allows high resolution measurements of energy losses and gains (phonons); the He diffuse scattering, due to the large scattering cross-section of isolated adatoms and defects, is very sensitive to disorder.

10.1 Background

The study of physisorbed rare gases has been shown to be a powerful tool in the understanding of elementary processes in surface physics, such as adsorption, desorption, melting or epitaxy [10.1]. In addition, physisorbed adlayers have acquired model character in the study of two-dimensional (2D) phases and their mutual transitions [10.2]. In analogy to bulk matter, these adsorbed layers can form quasi-2D gas, liquid or solid phases. Of particular interest are the solid phases; the substrate provides a periodic potential relief which interferes with the lattice structure of the monolayer, inducing modulations in the latter. In addition, since the adatoms belong to a different species than the substrate atoms, the strength of the lateral interactions within the adlayer differs in general from the strength of the adsorbate–substrate interaction. Depending on the delicate balance between these forces and on structural relationships, the adsorbed monolayer can form ordered solid structures which are commensurate (in registry) or incommensurate (out of registry) with the substrate (Fig.10.1).

Springer Series in Surface Sciences, Vol. 27 Helium Atom Scattering from Surfaces
Editor: E. Hulpke

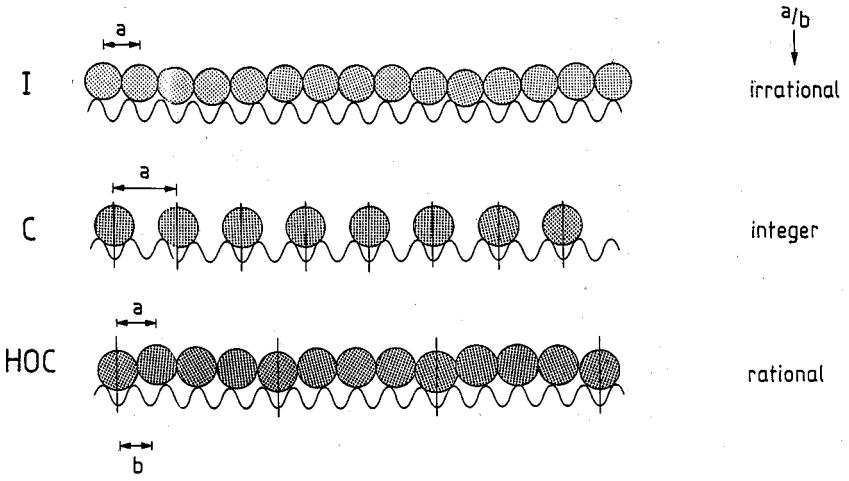

Fig.10.1. One-dimensional model of a physisorbed monolayer. The substrate is represented by a sinusoidal potential of period b and the adlayer by a chain of atoms with lattice constant a

When the periodic modulation of the adsorption potential in the directions parallel to the substrate surface (the so called corrugation of the substrate surface) is dominant, the adsorbed adatoms only occupy the energetically most favored sites and form a structure commensurate (C) with the underlying substrate. At the other extreme, when the adsorbate–adsorbate interaction dominates the periodic variation in the adsorbate–substrate interaction, the adlayer forms a structure which is determined by the dense packing of adatoms largely ignoring the substrate structure. This adlayer phase is termed incommensurate (I). Intermediate situations also occur when only a certain fraction of the adatoms occupies preferred adsorption sites; these are termed high order commensurate (HOC). The existence of these HOC phases has only recently been demonstrated experimentally. Only when the lateral adatom interaction and the substrate corrugation are comparable, can an ordered commensurate (C or HOC) adlayer undergo a transition into an incommensurate (I) phase as a function of coverage or temperature.

A variety of probe particles, such as electrons, neutrons, X-ray photons and thermal energy atoms are used as tools to investigate the structure of physisorbed films (cf. Ref. [10.2]). These methods of course all have their pros and cons. Low energy electron diffraction (LEED), for instance, is the most accessible technique, but suffers from the consequences of the strong interaction of the electrons with the adsorbed layer (multiple scattering, electron stimulated desorption etc.). Synchrotron X-ray scattering, on the other hand, has an excellent momentum resolution, but is hampered in application by its modest surface sensitivity.

The important characteristics of the He beam as a surface analytical tool are connected with the nature of the He–surface interaction potential. At large distances the He atom is subject to the weak attraction of the dispersion forces.

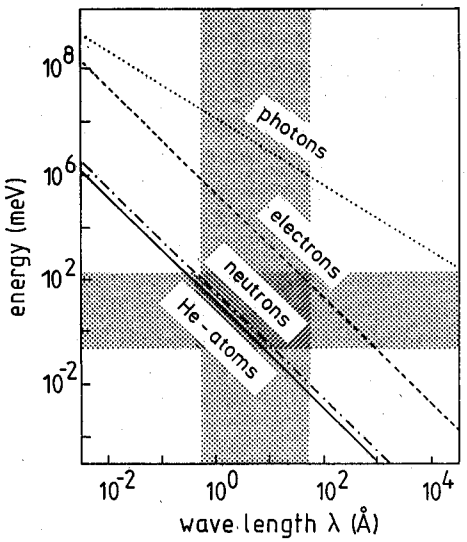

Fig.10.2. Energy-wavelength dispersion of common probe particles in surface scattering experiments. The shaded regions mark characteristic energy- and length-scales in surface processes

Upon closer approach, the electronic densities of the He atom and of the surface atoms overlap, giving rise to a strong repulsion. The classical turning point for thermal energy He is a few angstroms in front of the outermost surface layer. It is this interaction mechanism which makes the He atom sensitive exclusively to the outermost layer. The low energy of the He atoms and their inert nature ensures that He scattering is a completely nondestructive surface probe. This is particularly important when delicate phases, like physisorbed layers, are investigated. The de Broglie wavelength of thermal He atoms is comparable with the interatomic distances in adsorbed overlayers. Thus from measurements of the angular positions of the diffraction peaks the size and orientation of the two-dimensional (2D) unit cell, i.e., the structure of the outermost layer can be straightforwardly determined [10.3]. Analysis of the peak intensities yields the potential corrugation, which usually reflects the geometrical arrangement of the atoms within the 2D unit cell.

The energy of thermal He atoms is comparable with the energies of collective excitations (phonons) in overlayers. Thus, in a scattering experiment the He atoms may exchange an appreciable part of their energy with the surface [10.4]. This energy change can be measured in time-of-flight experiments with a resolution $\approx$ 0.3 meV; the resolution can even reach $\approx$ 0.1 meV (when using very low beam energies, $\simeq$ 8 meV). Thus, surface phonon dispersion curves of rare-gas layers can be mapped out by measuring energy-loss spectra at various momentum transfers in different crystallographic directions. This is a definite advantage of inelastic He scattering over inelastic neutron scattering. (In view of the random orientation of powdered samples, which have to be used in surface

investigations with neutron scattering, only average phonon density of states, but not dispersion curves can be obtained.) The range of energy transfer that can be covered by thermal He atoms is limited at the low end by the present maximum resolution of ≈ 0.1 meV and at the high end by the nature of the scattering mechanism. The thermal He-beam–surface interaction time being non-negligible, the upper limit for the observable phonon modes is ≈ 40 meV.

Besides the inelastic component, a certain contribution of elastically scattered He atoms is also found in between the coherent diffraction peaks. We will refer to this scattering as diffuse elastic scattering. This diffuse intensity is attributed to scattering from defects and impurities. Accordingly, this diffuse elastic scattering provides valuable information on the degree and nature of surface disorder. It can be used, for example, to study the growth of thin films [10.5] or to deduce information on the size, nature, and orientation of surface defects [10.6]. Very recently the TOF-peak width analysis of the diffuse elastic component has also been used to study the diffusive motion of adatoms [10.7].

Another remarkable way to use He scattering for the study of adsorbed layers is based on the large total cross section Σ for diffuse He scattering by isolated adsorbates (e.g., in the case of adsorbed Xe, $\Sigma_{\mathrm{Xe}}^{\mathrm{He}} \approx 110\text{Å}^2$ for $E_{\mathrm{He}} = 18$ meV) [10.8]. This large cross section is attributed to the long-range attractive interaction between adatom and the incident He atoms, which causes He atoms to be scattered out of the coherent beams. The large size of the cross section allows the extraction of important information concerning the lateral distribution of adsorbates, mutual interaction between adsorbates, dilute–condensed phase transitions in 2D, adatom mobilities, etc., simply by monitoring the attenuation of one of the coherently scattered beams, in particular of the specular beam [10.8]. This technique also allows the detection of impurities (including hydrogen!) in the ‰ range, a level hardly attainable with any other methods.

10.2 Experimental Aspects of Helium Scattering at Surfaces

Figure 10.3 shows schematically a He-atom–surface scattering experiment [10.9]: A highly monochromatic beam of thermal He atoms ($\Delta\lambda/\lambda \lesssim 0.01$) is generated in a high pressure supersonic expansion and collimated to a few tenths of a degree by a series of specially shaped collimators, the so called skimmers. Depending on source temperature (T_0), the wavelength of the He atoms ranges between $\lambda \approx 0.3$ and 2.0 Å; typical fluxes are of the order 10^{19} He atoms/s·sr:

$$E_{\mathrm{He}} = \frac{5}{2} k_{\mathrm{B}} T_0 \tag{101}$$

$$\lambda_{\mathrm{He}} = \frac{h}{\sqrt{2mE_{\mathrm{He}}}} \quad . \tag{10.2}$$

The time-of-flight spectrometers are designed to measure structural and dynamical surface properties in one experiment, i.e. designed to measure the double differential scattering cross section:

$$\frac{d^2\sigma}{d\Omega dE_f} = \frac{1}{I_0} \cdot \frac{\delta Z}{\delta E_f} \quad , \tag{10.3}$$

where δZ is the number of He atoms in the energy interval δE_f scattered into the solid angle element $\delta\Omega$, and I_0 the intensity of the incoming He beam. Except for trivial factors, the cross section is determined by the energy exchange ($\hbar\omega$) and the momentum exchange ($\boldsymbol{Q}$):

$$\frac{d^2\sigma}{d\Omega dE_f} \simeq S(\boldsymbol{Q}, \hbar\omega)$$

$$\hbar\omega = E_f - E_i, \quad \boldsymbol{Q} = \boldsymbol{k}_f - \boldsymbol{k}_i \quad . \tag{10.4}$$

Since the initial parameters of the incoming He beam and the geometry of the experiment are known, the energy and momentum transfer during the scattering can be calculated straightforwardly.

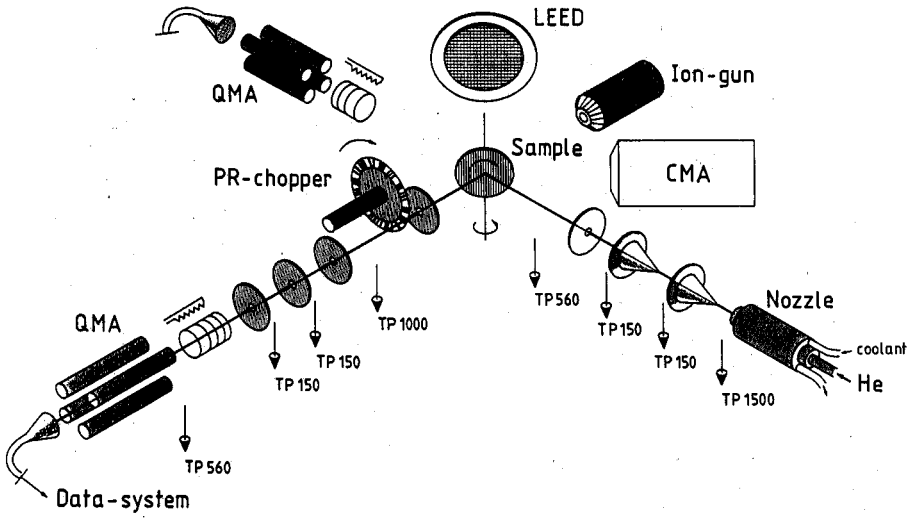

Fig.10.3. Schematic view of a high-resolution He–surface scattering spectrometer

The major experimental problems in high resolution He scattering are connected with the detection: large background and low detection efficiency. While with some technical effort the background can be efficiently reduced, no real breakthrough has been so far achieved in the attempt to increase the detection efficiency of He beams without impairing the time resolution. The method of choice is still electron bombardment ionization, followed by ion mass analysis.

The effective detection efficiency hardly surpasses 10^{-5}, with the time resolution still sufficient for time-of-flight He velocity analysis. Recent attempts to monitor the He metastables (also generated by electron bombardment) instead the He ions can be advantageous, when the He background pressure in the detector cannot be made low enough. In this type of detection, the relatively low efficiency is compensated by a favorable directionality effect: the He atoms in the beam are more efficiently detected than those in the isotropic background.

A relatively high He background is obviously inherent in all He beam experiments. Even a highly collimated beam puts a continuous, heavy He load on the pumps evacuating the sample chamber. In the case of the apparatus shown in Fig.10.3 the beam collimated to 0.2° (1.5×10^{-6}sr) supplies the sample chamber with about 1.5×10^{13} He/s (5.7×10^{-7} mbar· l/s). In view of some additional He load from the beam generator system and with a reasonably sized pumping system, the He background level in the sample chamber is rarely below 10^{-9} mbar. A detector located in this chamber would have a dynamical range of only $\sim 10^2$–10^3. This is acceptable when the information is inferred from the intense specular beam, but out of question when diffraction patterns of adlayers or inelastic scattering spectra are sought. The only practical way for a radical background reduction is the differential pumping. In the example in Fig.10.3, the scattering (sample) chamber is separated by three differential pumping chambers (one of them contains the chopper) which, together with the very efficient (high compression ratio) pumping of the detector chamber, leads to a He background pressure of $\sim 10^{-15}$ mbar in the latter. This results in an effective dynamical range of $\sim 10^6$. Very low intensity diffraction peaks (like second-order diffraction peaks from clean close packed metal surfaces) or weak inelastic resonances can be clearly resolved above the background.

The velocity distribution of atoms scattered from a surface is determined by measuring the time they need to cover a given distance (the so-called time-of-flight (TOF) method). The flight path is defined by the position of the chopper blade, which is preferably placed between sample and detector, and the center of the electron beam bombardment ionizer. For optimum resolution, the chopper opening function (gate function) should be in the ideal case a δ-function. The time interval between gate openings has to be large enough so that superpositions of slow and rapid atoms originating from successive openings can be neglected. The transmission is equal to the ratio between gate opening time and the interval between openings. Thus the width of the gate function, i.e. the time resolution, is a compromise between the ideal δ-function and an acceptable transmission which usually results in very low transmission values (of order 0.1%) for reasonable time resolutions.

An elegant and efficient alternative is the use of pseudorandom chopping. This method was first introduced in inelastic neutron scattering studies in the late 1960s. The gate function is a "pseudorandom" sequence of slots and bars. We use in our laboratory a binary shift register sequence of 512 slots and 511 bars, of 2.5 μs width each (at a rotor speed of 391 Hz). The distribution of arrival times is deconvoluted to the TOF distribution by cross-correlation. A detailed description of the pseudorandom TOF technique can be found in

[10.10–12]. The transmission is close to 50%, independent of time resolution. The stringent requirements of a highly constant rotation period of the chopper during the whole measuring time and a very low phase jitter (smooth rotation) of the chopper during each revolution are not easy to satisfy under UHV conditions. This has been realized, however, by using a chopper with magnetic bearings.

A matter of controversial discussion is the comparison of pseudorandom and conventional single slot chopping; for details see [10.12]. The comparison can be expressed quantitatively by introducing the gain factor $G(f_k)$, which represents the ratio of the variances resulting in channel k from the two kinds of chopping. For binary shift register sequences, the gain factor is given by

$$G(f_k) = \frac{\sigma^2_{\text{single-slot}}}{\sigma^2_{\text{pseudorandom}}} \simeq \frac{1}{2}\frac{f_k + \bar{u}}{\bar{f} + \bar{u}/n} \quad ,$$

where f_k is the number of counts of the time-dependent signal in channel k, $\bar{f}$ is its mean value, $\bar{u}$ is the mean number of counts per channel of the time-independent signal (the real background), and n the number of slots of the pseudorandom sequence. The pseudorandom chopping is favoured when $G(f_k) > 1$. This is always the case when $\bar{u} > 2\bar{f}$ because $n \gg 1$. The general interest, so far, is focussed on the position, height, and shape of the peaks in the TOF spectra and much less on the shape of a possibly present energy-dependent background. In this case a much less restrictive condition can be deduced: the pseudorandom chopping is favoured when in the "interesting" channels $f_k > 2\bar{f}$, irrespective of the value of $\bar{u}$. This condition is fulfilled for all significant peaks and thus the pseudorandom chopping is of advantage, even if technically more demanding.

The effective resolution of the He-scattering spectrometer as a whole is in fact the figure of primary interest. For the spectrometer used in the authors' laboratory the overall instrumental resolution (taking into account the scattering geometry, chopper gate function, energy spread of the incoming He-beam and the finite length of the ionization region) amounts to $\approx 7\mu$s FWHM for a typical flight time of 800 μs corresponding to 0.32 meV FWHM at a 18 meV beam energy. The characteristic parameters of the high resolution He spectrometers HETOF–1 and –2 run in our laboratory in Jülich are summarized in Table 10.1. Today, there are about ten high resolution He spectrometers of similar characteristics in operation (Chicago–Sibener, Genua–Tatarek, Göttingen–Toennies, Murray Hill–Doak).

The capabilities of such a high resolution instrument are demonstrated in Figs.10.4 and 10.5. In Fig.10.4 we show as an example a He diffraction scan from a complete Xe monolayer adsorbed on Pt(111) ($\Theta_{\text{Xe}} \approx 0.42$ Xe atoms per Pt substrate atom); a well behaved diffraction pattern with sharp Bragg peaks is observed. This diffraction scan has been measured in a fixed scattering geometry $\theta_f + \theta_i = 90°$ by rotating the Pt crystal around an axis perpendicular to the scattering plane; the angle on the abscissa is transformed to the parallel momentum transfer scale by the relation $Q^{\parallel} = 5.723(\sin\theta_f - \cos\theta_f)$. The

Table 10.1. Characteristics of the high resolution He time-of-flight spectrometers operated in Jülich

Beam energy:	2–170 meV	
Beam energy spread:	$\Delta E/E = 2\Delta\lambda/\lambda =$	
	0.014	($E_{He} = 18$ meV)
	0.020	($E_{He} = 69$ meV)
Beam intensity:	$\sim 10^{19}$ He atoms/s·sr	
Detector sensitivity:	$\geq 3 \cdot 10^{-5}$	
Transfer width:	~ 400Å for $\theta_i = \theta_f = 45°$	
Spectrometer energy resolution:		
	0.32 meV	($E_{He} = 18$ meV)
	1.70 meV	($E_{He} = 69$ meV)

diffraction pattern characterizes a hexagonal close packed 2D Xe crystalline solid with a nearest neighbor distance of 4.33 Å. In the inset of Fig.10.4 the orientational structure (with respect to the Pt substrate) of the Xe monolayer is characterized in an azimuthal diffraction profile, which is obtain by rotating the Pt crystal around its surface normal at a fixed polar angle corresponding to a Bragg position. The symmetric peak-doublet centered along the $\bar{\Gamma}\bar{K}_{Pt}$ direction of the substrate surface characterizes a Novaco–McTague rotated phase rotated ±3.3° off the natural R30° orientation of submonolayer Xe films. The tiny satellite-peak at $Q \sim 0.3$ Å^{-1} with an intensity of about 10^{-5} of the incident beam has been identified as the mass-density-wave (MDW) satellite of the rotated Xe monolayer [10.13]. These diffraction satellites which arise due to a periodic deviation of the positions of monolayer atoms from their regular lattice sites in the rotated phase have been looked for since its original prediction in 1978 by *Novaco* and *McTague* [10.14] but were not observed with the classical diffraction techniques (electrons, neutrons, X-ray). It is indeed the high sensitivity of thermal He atoms to very small modulations of the adlayer topography which allows the detection of MDW satellites in a diffraction experiment.

The resolving power of inelastic He scattering is demonstrated in Fig.10.5. A series of TOF spectra taken from a full Ar monolayer on Pt(111) at different scattering angles are plotted over an energy-loss range from −2 to −6 meV. In these spectra the various features of the dynamical coupling between the adlayer and Pt substrate [10.15] can be distinguished. As a reference, let us first look at the spectrum (d) taken at $\theta_i = 35°$ which corresponds to the creation of an Ar monolayer phonon with wave vector $Q = 0.78$Å^{-1}, i.e., close to the edge of the 2D Ar Brillouin zone [$Q(\bar{M}) = 0.98$Å^{-1}]. Since at these large Q values the Pt Rayleigh wave and the Pt bulk phonons have much higher energies than the Ar adlayer mode, no coupling of the Ar phonons to the Pt substrate is expected here. Indeed, the small linewidth $\Delta E = 0.32$ meV of the Ar loss peak at −4.8 meV is determined only by the instrumental resolution ΔE_{instr} of the spectrometer without any measurable additional broadening. Spectrum (a)

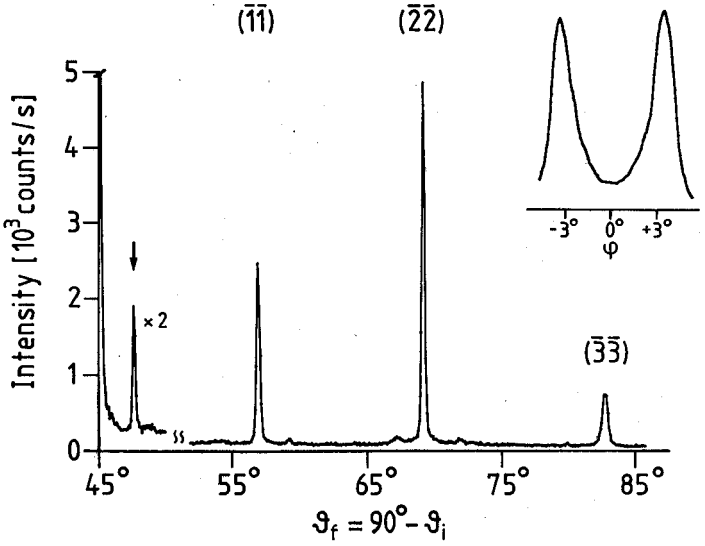

Fig.10.4. Polar and azimuthal (inset) He diffraction scan of a complete Xe monolayer on Pt(111); He wavelength $\lambda = 1.098$Å, surface temperature 25 K. The polar scan is taken along the $\bar{\Gamma}\bar{M}_{Xe}$-azimuth

exhibits two-phonon loss peaks. The feature at -2.9 meV is a signature of the Pt Rayleigh wave dynamically coupled to the Ar adlayer mode. Furthermore, the Ar loss at -5.0 meV is much broader ($\Delta E \simeq 0.41$ meV) than in spectrum (d). This difference is due to the fact that the Ar phonon in (a) is created at the center of the Brillouin zone $\bar{\Gamma}$ ($Q = 0.0/\text{Å}^{-1}$) where an effective damping of the Ar phonons due to the coupling to the projected bulk phonon bands of the Pt substrate occurs. This so called "radiative damping" of the adlayer phonon results in a linewidth broadening $\varepsilon \equiv \left[(\Delta E)^2 - (\delta E_{\text{instr}})^2\right]^{1/2}$ of 0.2–0.3 meV. It is instructive to estimate the corresponding lifetime shortening due to this radiative damping. Using the Heisenberg uncertainty principle $\varepsilon \Delta t = h$ the lifetime becomes $\Delta t \sim 3 \times 10^{-12}$ s. Relating this value to the time scale of the Ar–Pt vibration $\hbar\omega = 5.0$ meV, i.e., $\nu = 1.2$ THz, a mean phonon lifetime of about three vibrational periods is obtained. Besides the radiative damping also the hybridization of the Ar adlayer mode and the Pt Rayleigh wave is observed. This is shown in spectrum (c) of Fig.10.5. At these scattering conditions ($\theta_i = 37.7°$) corresponding to a wave vector $Q = 0.45\text{Å}^{-1}$ of the Ar phonon, the crossing of the adlayer mode and the Pt Rayleigh wave should occur. Instead, due to the hybridization of the two modes this crossing is avoided and a phonon doublet with an energy splitting of ~ 0.8 meV is observed (note also the comparable heights of the two peaks). Details of the dynamical coupling between an adsorbed layer and the substrate and of the phonon spectrum of thin physisorbed films (1–25 monolayers) can be found in [10.16–18]. The high energy resolution of the spectrometer at sufficiently high

primary energies (ΔE = 0.32 meV at E_{He} = 18.3 meV) recently enabled us to measure for the first time the intrinsic linewidth of a surface phonon and its temperature dependence [10.19].

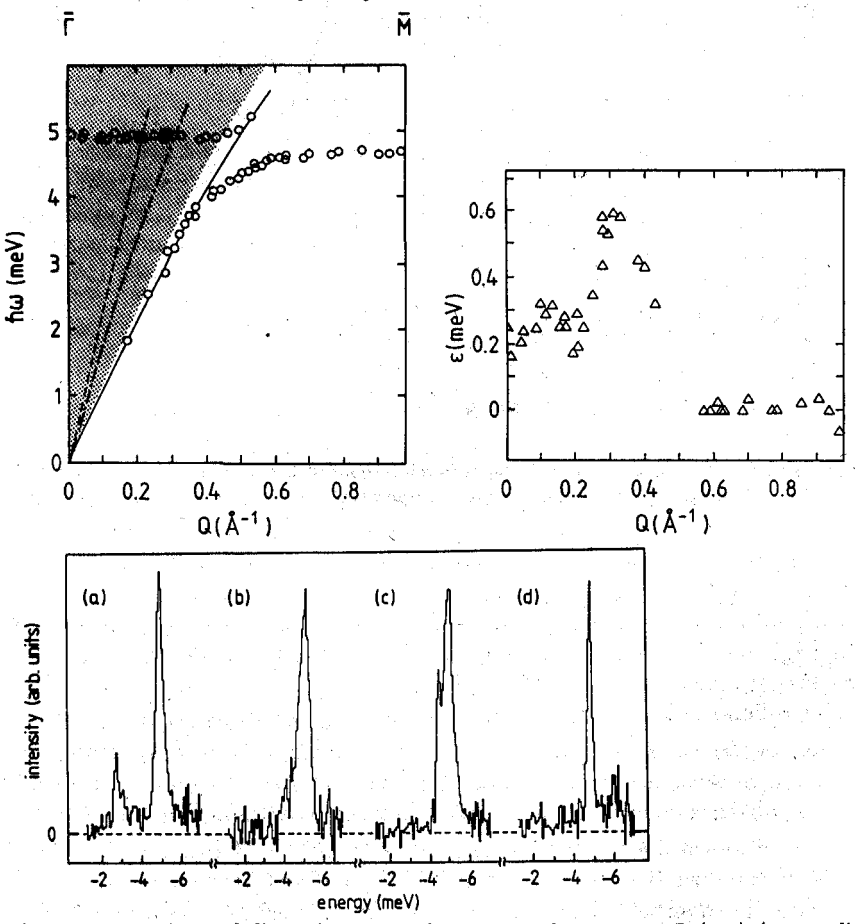

Fig.10.5. Experimental dispersion curves from a monolayer Ar on Pt(111) (perpendicular polarized mode) and He TOF spectra (inset) taken at different incident angles θ; along the $\bar{\Gamma}\bar{M}$ direction of the Ar unit cell: (a) 40.4°, (b) 38.5°, (c) 37.7°, (d) 35°. The energy of the primary He beam was 18.3 meV

10.3 Rare Gas Monolayer Phases on Pt(111)

10.3.1 Isolated Adatoms and the 2D Gas → 2D Gas + 2D Solid Phase Transition

For the perfect (111) surface of the fcc metal platinum, the corrugation sensed by a He atom of thermal energy is extremely small, giving rise to diffraction intensities of less than 10^{-4} of the specularly reflected intensity: a close-packed metal surface acts as an almost perfect mirror for thermal energy He-atoms. Adsorption on clean surfaces results in a dramatic decay of the specular intensity; the mirror becomes blind. From the initial slope of the adsorption curve (specular intensity versus coverage) it is possible to define a total scattering cross section for diffuse scattering Σ, associated with one adatom [10.20]:

$$\Sigma = -\frac{1}{n_s} \cdot \left.\frac{d(I/I_0)}{d\Theta}\right|_{\Theta=0} , \tag{10.5}$$

where I and I_0 are the intensities of the specular beam of the adsorbate covered and the clean surface, respectively, Θ is the adsorbate coverage, defined as the number of adatoms per Pt surface atom and n_s is the first layer Pt atom density. The experimental Σ values, determined through (10.5) are of the same order as gas phase total scattering cross sections ($\approx 100\text{Å}^2$). This large cross section is attributed to the long range attractive interaction between the adatom and the incident He atom, which causes the He atoms to be scattered out of the coherent beams. The remarkable size of the cross section, 4–6 times the geometrical size, A, of the adsorbate allows the extraction of important information concerning the lateral distribution of adsorbates, mutual interactions between adsorbates, dilute–condensed phase transitions in 2D, adatom mobilites, etc., simply by monitoring the attenuation of one of the coherently scattered beams.

As mentioned above the possibility to investigate the lateral distribution of adsorbates, in particular the dilute–condensed phase transition in 2D, is based upon the large difference between the cross section for diffuse scattering, Σ, and the geometrical size, A, of the adsorbates. The degree of overlap of the cross sections Σ at a certain adsorbate coverage Θ which determines the surface reflectivity, depends on the nature of the lateral distribution of the adsorbate. For instance, as long as the adsorbates form a lattice gas, the surface reflectivity for He atoms depends on Θ according to

$$\frac{I}{I_0} = (1-\Theta)^{\Sigma n_s} \tag{10.6}$$

$$\frac{I}{I_0} \simeq 1 - \Sigma n_s \, \Theta \quad \text{for } \theta << \Sigma n_s \quad . \tag{10.6.1}$$

On the other hand, when island formation starts, i.e. at the 2D gas → 2D solid transition, the reflectivity is determined by the much smaller geometrical size A of the adatoms in the 2D condensed phase:

$$\frac{I}{I_c} \simeq 1 - An_s(\Theta - \Theta_c) \quad , \tag{10.7}$$

with I_c being the specular intensity at the critical coverage Θ_c, where condensation sets in. A comparison of (10.6) and (10.7) shows that, when condensation sets in, the slope of the specular He intensity I versus coverage Θ is expected to change dramatically: the ratio $\Sigma/A \simeq 4$–6. This is illustrated in Fig.10.6 for a Pt(111) surface at 54 K exposed to Kr at $p_{Kr} = 2.1 \times 10^{-9}$ mbar.

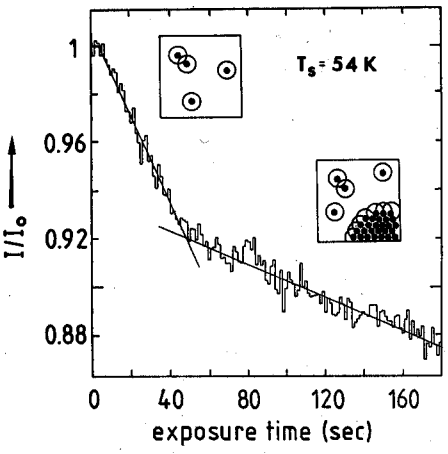

Fig.10.6. Specularly reflected He intensity from a Pt(111) surface at 54 K during exposure to $p_{Kr} = 2.1 \times 10^{-9}$ mbar

The sudden slope change in Fig.10.6 obviously marks directly the onset of islanding. The critical coverage Θ_c corresponds to the 2D vapor pressure of Kr on Pt(111) at 54 K. From measurements of Θ_c at different temperatures, the 2D latent heat of vaporization is obtained under the assumption that the 2D gas is nearly perfect. In Table 10.2 the 2D latent heats of vaporization obtained in this way for Xe, Kr, and Ar on Pt(111) are listed. They actually represent the lateral interaction energy between the adlayer atoms.

Table 10.2. Lateral interaction energies for rare gases adsorbed on Pt(111)

adatom	Xe	Kr	Ar
ε_ℓ [meV]	43	26	17

10.3.2 Commensurate, High Order Commensurate and Incommensurate Adlayers

When the lateral adatom interaction and the substrate corrugation are comparable, the adsorbed monolayer may form various ordered structures, commensurate as well as incommensurate phases, allowing the investigation of the corresponding CI transition as a function of coverage or temperature. This CI transition is driven by the formation of line defects, so called misfit dislocations as was demonstrated first by *Frank* and *van der Merwe* [10.21]. These authors studied a linear chain of atoms with a lattice constant placed in a sinusoidal potential of amplitude V and periodicity b, representing the mutual interactions of the atoms in the chain by springs with spring constant K. The calculations reveal that for slightly different lattice parameters of chain and substrate, i.e. for a weakly incommensurate adlayer, the lowest energy state is obtained for a system which consists of large commensurate domains separated by regions of bad fit. The regions of poor lattice fit are dislocations with Burgers vectors parallel to the chain.

In two-dimensional systems these regions of bad fit (the domain walls) are lines. Because in a triangular lattice there are three equivalent directions, domain walls can cross. Using Landau theory, *Bak* et al.[10.22] have shown that it is the wall crossing energy Λ which determines the symmetry of the weakly incommensurate phase and the nature of the phase transition. For attractive walls, $\Lambda < 0$, a hexagonal network of domain walls (HI) will be formed at the CI transition because the number of wall crossings tends to be as large as possible. This C–HI transition is predicted to be first order. For repulsive walls, $\Lambda > 0$, the number of wall crossings tends to be as small as possible, i.e. a striped network of parallel walls (SI) will be formed in the incommensurate region. The C–SI transition is predicted to be continuous. The striped phase is expected to be stable only close to the CI phase boundary. At large incommensurabilities the hexagonal symmetry should be recovered in a first order SI–HI transition. In Fig.10.7 we summarize the possible domain wall structures. Superheavy and heavy walls are characteristic for those systems in which the incommensurate phase is packed more densely than the commensurate phase, while for light and superlight walls the opposite holds.

The best known examples of the CI transition in 2D adlayer systems are those which occur in the Kr monolayer on the basal (0001) plane of graphite [10.23] and in the Xe monolayer on the Pt(111) [10.2,24] surface. Here we will discuss briefly the physics of the Xe/Pt system (Fig.10.8). Below coverages of $\Theta_{Xe} \simeq 0.33$ and in the temperature range 60–99K, xenon condenses in a $(\sqrt{3} \times \sqrt{3})$R30° commensurate solid phase. This phase has sharp diffraction peaks characteristic for coherent Xe domains which are about 800 Å in size. As the coverage is increased above 0.33 the relatively loosely packed Xe structure ($\approx$ 9% larger lattice constant than in bulk Xe) undergoes a transition from the commensurate $\sqrt{3} \times \sqrt{3}$ structure to an incommensurate striped solid phase with superheavy walls. This weakly incommensurate solid is able to accommodate more Xe atoms than the commensurate phase by dividing into regions of

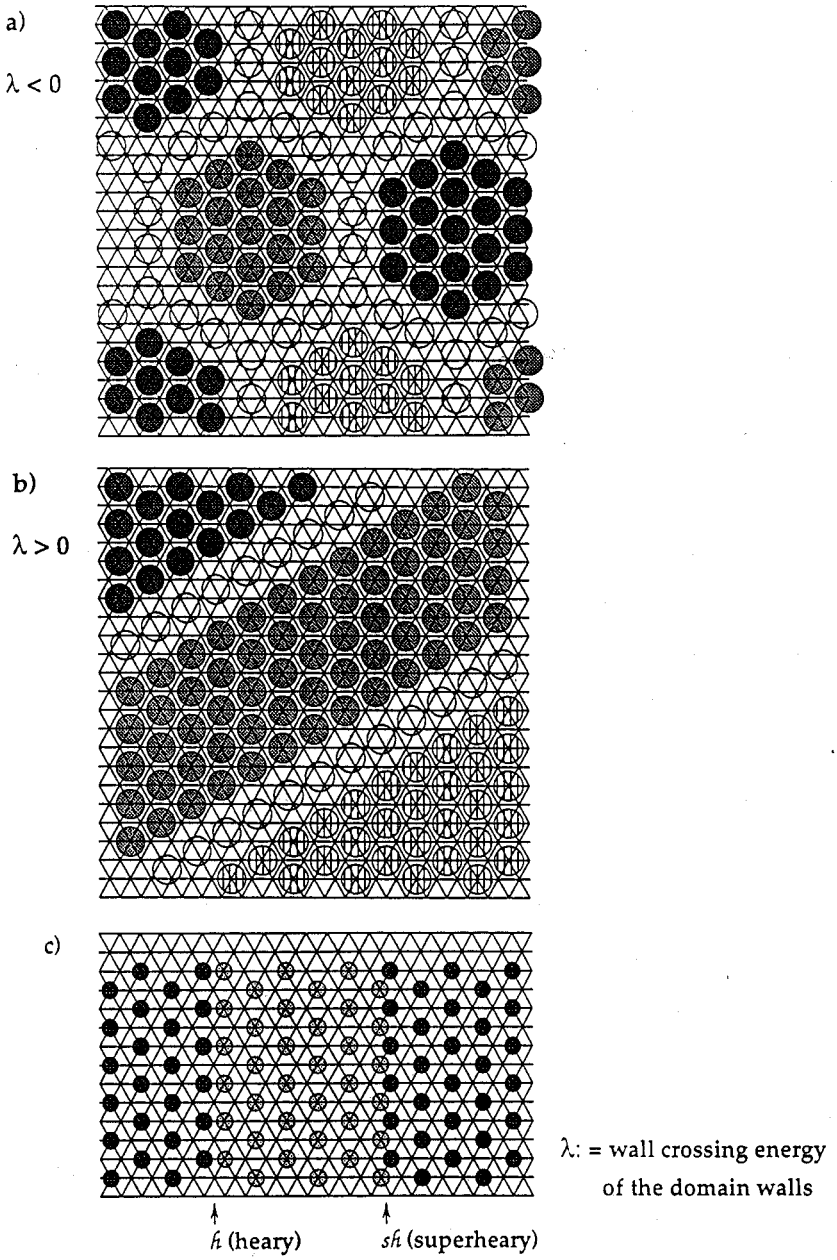

Fig.10.7. Domain wall systems for a $(\sqrt{3} \times \sqrt{3})$R30° phase on a triangular substrate lattice; the walls are of the "light" type

commensurate domains separated by a regularly spaced array of striped denser domain walls. Increasing coverage causes the commensurate domains to shrink and brings the walls closer together. The domain walls are thus a direct consequence of the system's efforts to balance the competition between the lateral Xe–Xe and the Xe–Pt interactions. The C–SI transition can also be induced by decreasing the temperature below $\sim$ 60K at constant coverage $\Theta_{Xe} < 0.33$; the driving force for this temperature-induced CI transition being anharmonic effects [10.25].

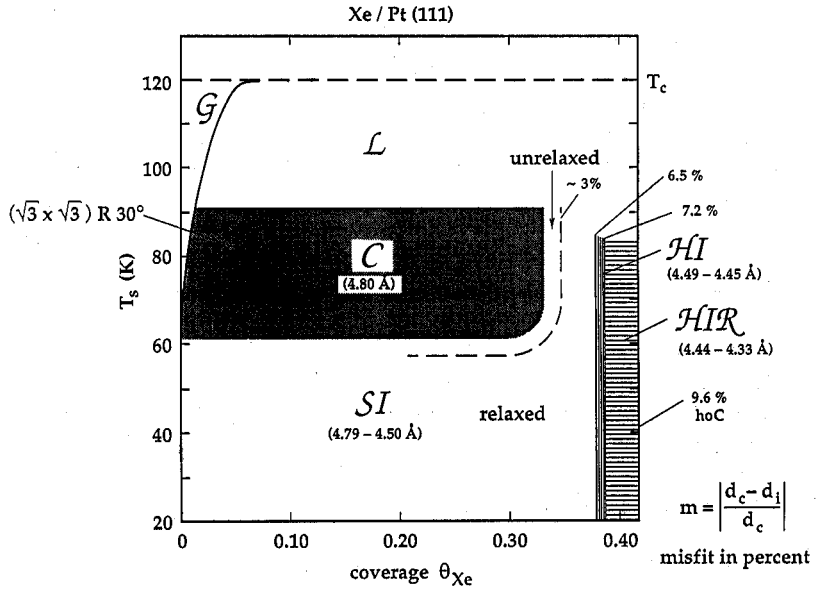

Fig.10.8. Schematic phase diagram of monolayer Xe on Pt(111). C, SI, HI, HIR denote the commensurate $(\sqrt{3} \times \sqrt{3})$R30°, the striped incommensurate, the hexagonal incommensurate and the hexagonal incommensurate rotated 2D solid phases. *G* and *L* denote the 2D gas and liquid, respectively

The usual measure for the incommensurability of an I phase is the misfit $m = (a_c - a_i)/a_c$, where a_c is the lattice parameter of the commensurate phase and a_i that of the incommensurate structure. For striped I phases, the misfit has of course uniaxial character, being defined only along the direction perpendicular to the domain walls. Quantitative measurements of the misfit during the C–SI transition of Xe on Pt(111) have revealed a power law of the form

$$m = \frac{1}{\ell} \propto (1 - T/T_c)^{0.51 \pm 0.04} \quad , \tag{10.8}$$

i.e. the distance ℓ between nearest neighbor walls scales with the inverse square root of the reduced temperature. This square-root dependence is the result of

an entropy-mediated repulsion between meandering nearest neighbor walls and is in accord with theoretical predictions [10.26].

With increasing incommensurability the domain wall separation becomes progressively smaller until at a critical misfit of $\sim$ 6.5% the Xe domain wall lattice rearranges from the striped to the hexagonal symmetry (Fig.10.7) in a first order transition [10.27]. A further increase of the incommensurability by adding more and more Xe eventually results in an adlayer rotation to misalign itself with the substrate in order to minimize the increasing strain energy due to the defect concentration [10.27]. This continuous transition to a rotated phase (HIR) follows a power law $\varphi \propto (m - 0.072)^{1/2}$ starting at a critical separation between nearest neighbor walls $\ell_c \simeq 10$ Xe-row distances (see also Fig.10.4).

It is generally accepted that on the same substrate the absolute magnitude of the corrugation increases with the size of the rare gas adatom, while the corrugation decreases relative to the binding energy of the adatom as well as relative to the lateral adatom interaction [10.28]. Thus, within our simple model of competing interactions (corrugation versus lateral attraction) we expect a gradual transition from the floating Xe monolayer with its rich diversivity of incommensurate domain wall phases to locked Kr or Ar layers which are dominated by the lock-in forces of the substrate, favoring HOC phases instead of incommensurate domain wall phases.

Until recently, there has been no convincing experimental evidence for the existence of high order commensurate physisorbed layers. This appeared to support the widespread belief that "experimentally it is impossible to distinguish between a high-order C structure and an incommensurate structure" (Per Bak in Ref.[10.29]).

This belief is certainly legitimate if the only accessible experimental information is the ratio of the adlayer and substrate lattice basis vectors. Indeed, because one can always find a rational number within the confidence range of any experimental irrational number, i.e. the basis vectors supplied by the most refined experiment are always compatible with a high (enough) order commensurate phase. There are, however, two other experimentally accessible parameters which allow a unequivocal distinction between a high order commensurate "locked" and an incommensurate "floating" layer [10.30]. First: the superstructure formed by the atoms located in equivalent, energetically favorable high symmetry sites. These more strongly bound atoms being located "deeper" in the surface than the others, the adlayer is periodically buckled. Because of the extreme sensitivity of He scattering to the surface topography, this superstructure, which characterizes high order commensurate layers, is directly accessible to a high resolution He diffraction experiments. Second: the thermal expansion. Indeed, a "floating" layer is expected to thermally expand very much like the corresponding rare gas bulk crystal, while a "locked" layer has by definition to follow the substrate to which it is locked. The thermal expansion of rare gas solids is at least ten times larger than that of substrates normally employed, and so the distinction between high order commensurate "locked" and incommensurate "floating" becomes straightforward. This very sharp criterion requires that the "locking" is strong enough to withstand temperature

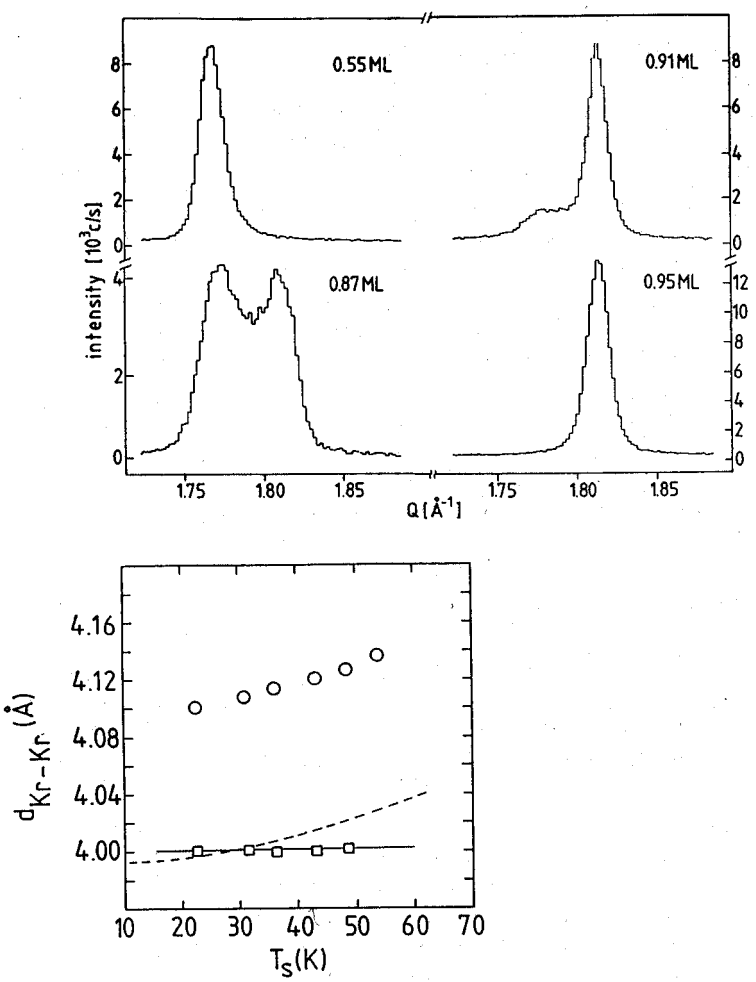

Fig.10.9. a) Polar He-diffraction scans of the $(1,1)_{Kr}$ -diffraction order from Kr adlayers on Pt(111) at various Kr submonolayer coverages at $T_s = 25K$. b) Kr-layer lattice spacing vs T_s for the () high (0.95 ML) and (o) low (0.5 ML) coverage phase; temperature dependence of the lattice spacing of (—) Pt-substrate, and of (- - -) bulk Kr

variations over a sufficently large range ($\geq$ 10K) to allow for reliable thermal expansion measurements.

Figure 10.9a shows a series of polar He scans of the (1,1)Kr diffraction peak taken at 25 K along the $\bar{\Gamma}\bar{M}_{Kr}$ direction of the Kr monolayers adsorbed on a Pt(111) surface at coverages between 0.5 and 0.95 ML. The sequence is characteristic for a first order phase transition from a hexagonal solid phase with wavevector $Q = 1.769\text{Å}^{-1}$ ($d_{Kr} = 4.10\text{Å}$) to one with $Q = 1.814\text{Å}^{-1}$ ($d_{Kr} = 4.00\text{Å}$), below and above 0.8 ML, respectively. Dur-

ing the phase transition the intensity diffracted from one phase increases at the expense of the other.

The question concerning the incommensurate "floating" versus high order commensurate "locked" nature of the two Kr phases has been addressed by looking at their thermal expansion behavior and by searching for superstructure satellites. In Fig.10.9b the measured Kr–Kr interatomic spacing versus temperature is shown for submonolayer films of coverage 0.5 ML and 0.95 ML. The difference is striking. The low coverage phase shows a variation with temperature, very much like bulk Kr (dashed) and is thus an incommensurate "floating" phase. On the contrary, the lattice parameter of the high coverage phase is — like that of the Pt substrate (solid) — constant within experimental error in the same temperature interval; accordingly, this Kr-phase is high order commensurate "locked".

This assignment is supported by inspection of Fig.10.10, where polar scans (He energy 12 meV) in the $\bar{\Gamma}\bar{M}_{Kr}$-direction of the "floating" and of the "locked" Kr layer are shown. The scans differ substantially: the locked scan clearly evidences the presence of a superstructure, while the floating one does not. The superstructure peak at $Q = 0.532 \pm 0.022\text{Å}^{-1}$ corresponds to 1/5 of the Pt substrate principal lattice vector. The origin of the superstructure peak is illustrated on the right hand of Fig.10.10 where the "locked" Kr phase on the Pt(111) surface is schematically shown. The Kr layer is rotated by 30° with respect to the substrate and its translational position is fixed by locating the central Kr atom in a preferred three fold hollow site (say fcc). Obviously, the Kr atoms in fcc sites (filled small circles) form a hexagonal (5×5)R0°-superstructure which is responsible for the diffraction satellite at $Q_{Pt}^{(1,1)}$. Note that the superstructure is aligned with the substrate lattice while the Kr layer as a whole is rotated by 30°; this is the reason while the superstructure satellite is seen in the $\bar{\Gamma}\bar{M}_{Pt} = \bar{\Gamma}\bar{M}_{Kr} = \bar{\Gamma}\bar{M}_{superstructure}$-direction. The particular ratio between the lattice parameters of adlayer and substrate $\sqrt{3}d_{Pt}/d_{Kr} = 6/5$ produces an additional pecularity; the same number of Kr atoms are located in hcp and fcc hollow sites. Thus, the (5×5)R0° -superstructure has a two-atomic basis. A simple counting in Fig.10.10 shows that one sixth of the Kr atoms are locked in a hollow site (fcc or hcp). This fraction appears to be sufficient to prevent the Kr layer from expanding freely over more than 25 K.

10.3.3 Influence of Extrinsic Defects

Almost any theoretical study of adsorbed layers deals with perfect substrates, i.e. strictly periodic arrangements of surface atoms extending over infinite distances. In experiment, however, this situation is almost never met. Indeed, unavoidable slight misorientations of the substrate plane with respect to the low-index planes during crystal surface preparation result in a finite step density. Today's best prepared low-index metal surfaces have step densities of $\approx 0.1\%$, corresponding to average domain sizes of perfect coherence of $\approx$ 2000–3000Å. In addition, even under the most careful experimental ultrahigh vacuum conditions (base pressure in the low 10^{-11} mbar range), small amounts of adsorbing

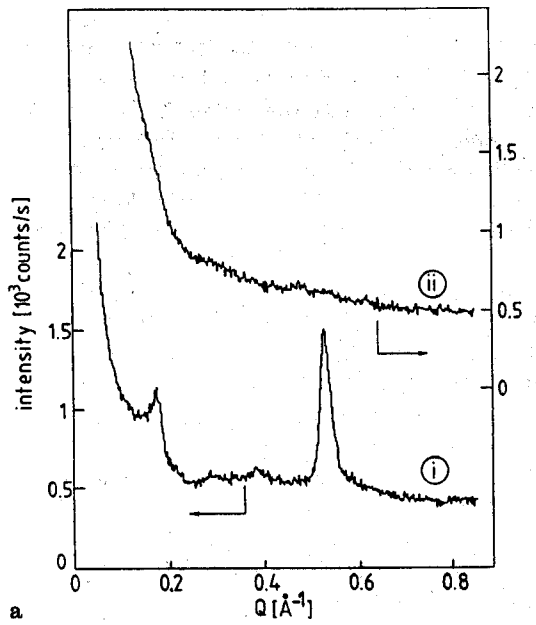

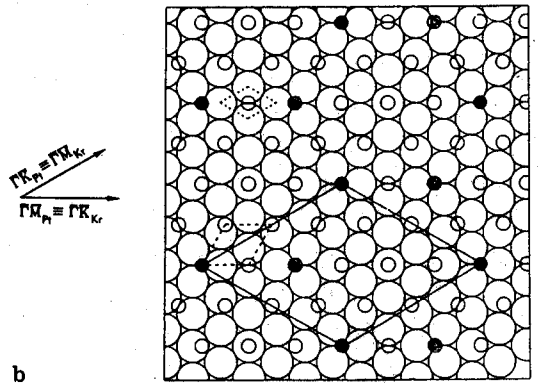

Fig.10.10. (a) Polar He diffraction scans of Kr monolayers in the vicinity of the specular peak ($Q = 0\text{Å}^{-1}$); (i) high (0.95 ML) and (ii) low (0.5 ML) coverage phase, taken along the $\bar{\Gamma}\bar{M}_{Kr}$ -azimuth. (b) Schematic representation of the high coverage phase of Kr on Pt(111); small circles represent Kr-atoms ($d_{Kr-Kr} = 4.00$Å) while large circles the Pt substrate atoms ($d_{Pt-Pt} = 2.77$Å).

impurities (H_2O, H_2, CO) cannot be completely avoided. These extrinsic defects can have a dramatic influence on phase transitions of adsorbed layers [10.31].

We have demonstrated recently that depending on the presence or absence of minute amounts ($\approx 0.1\%$) of preadsorbed impurities, Kr monolayers may be aligned (R0°) or rotated by 30°(R30°) with respect to the Pt(111) substrate, respectively [10.32]. We have been able to demonstrate in a direct experiment that when the Kr atoms are allowed to nucleate at the residual $\sim 0.1\%$ step sites of the substrate (the binding energy at step sites is $\sim 25\%$ larger than on terrace sites [10.33]) the R30° orientation is obtained; in contrast, when the step sites are blocked by preadsorbed CO (or H, or even Xe) the growing Kr layer cannot nucleate at step sites leading to an orientation aligned (R0°) with the substrate.

To prepare Pt(111) surface with the CO-decorated steps we have taken advantage of the cross-section overlap of admolecules (CO) and defects (steps). If the CO molecules are located at a terrace they contribute with their full diffuse cross section to the attenuation of the specular beam $\Sigma_{CO}^{eff,terrace} \approx \Sigma_{CO}$, while CO molecules at step edges have a much lower cross section $\Sigma_{CO}^{eff,step} \ll \Sigma_{CO}$. This approach [10.34] is demonstrated in Fig.10.11

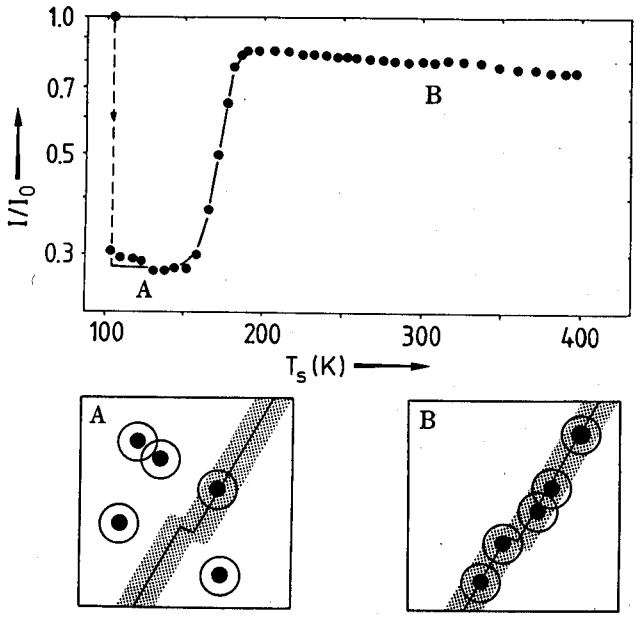

Fig.10.11. Relative He specular intensity I/I_0 versus surface temperature T_s. I is monitored starting with the clean Pt(111) surface at $T_s = 107$K, then during CO adsorption and finally during the linear heating (0.4 K/s) of the surface. The data are corrected for Debye-Waller effects

First the surface is cooled to a low enough temperature ($T < 130$K) to ensure that the CO admolecules are immobile. A small quantity of CO molecules

is now adsorbed. Terrace and step sites are stochastically covered upon adsorption. Obviously, the CO molecules on terrace sites contribute mostly to the attenuation of the specular He beam; because of the strong overlap with the cross sections of the step atoms the effective contribution to attenuation of the CO molecules on step sites is minor. Finally, the surface is heated linearly and the intensity of the specular He beam monitored continuously. As soon as the CO molecules on the ideal terrace sites become mobile on the timescale of the heating rate, they migrate and are eventually trapped at step sites. The ideal terrace sites (the He mirror) become largely adsorbate free and thus the intensity of the specular He beam increases almost to the clean surface value. The overlap mechanism makes the migration from terrace to step sites directly visible. From the shape of the curve in Fig.10.11 we can also deduce an activation energy for CO diffusion on Pt(111); in the framework of a simple hopping model a value $E_{\mathrm{diff}} \approx 7$ kcal/mol is obtained [10.34].

References

10.1 S.K. Sinha (Ed.): *Ordering in Two Dimensions* (North Holland, Amsterdam 1980)
10.2 K. Kern, G. Comsa: In *Chemistry and Physics of Solid Surfaces* VII, ed. by R. Vanselow, R.F. Howe, (Springer, Berlin Heidelberg 1988) p.65
10.3 T. Engel, K.H. Rieder: *Structural Studies of Surfaces with Atomic and Molecular Beam Diffraction*, Springer Tracts Mod. Phys., Vol. 91 (Springer, Berlin, Heidelberg 1982)
10.4 J.P. Toennies: J. Vac. Sci. Technol. A **2**, 1055 (1984)
10.5 K. Kern, R. David, R.L. Palmer, G. Comsa: Phys. Rev. Lett. **56**, 2823 (1986)
10.6 A.M. Lahee, J.R. Manson, J.P. Toennies, Ch. Wöll: Phys. Rev. Lett. **57**, 471 (1986)
10.7 J.W. Frenken, J.P. Toennies, Ch. Wöll: Phys. Rev. Lett. **60**, 1727 (1988)
10.8 G. Comsa, B. Poelsema: Appl. Phys. A **38**, 153 (1985)
10.9 R. David, K. Kern, P. Zeppenfeld, G. Comsa: Rev. Sci. Instr. **57**, 2771 (1986)
10.10 G. Comsa, R. David, B.J. Schumacher: Rev. Sci. Instr. **52**, 789 (1981)
10.11 K. Sköld: Nucl. Instr. Meth. **63**, 114 (1968)
10.12 L.K. Verheij, P. Zeppenfeld: Rev. Sci. Instr. **58**, 2138 (1987)
10.13 K. Kern, P. Zeppenfeld, R. David, G. Comsa: J. Vac. Sci. Technol. A **6**, 639 (1988)
10.14 A.D. Novaco, J.P. McTague: Phys. Rev. B **19**, 5299 (1979)
10.15 B. Hall, D.L. Mills, J.E. Black: Phys. Rev. B **32**, 4932 (1985)
10.16 K. Kern, P. Zeppenfeld, R. David, G. Comsa: Phys. Rev. B **35**, 886 (1987)
10.17 B. Hall, D.L. Mills, P. Zeppenfeld, K. Kern, U. Becher, G. Comsa: Phys. Rev. B **40**, 6326 (1989)
10.18 P. Zeppenfeld, U. Becher, K. Kern, R. David, G. Comsa: Phys. Rev. B **41**, 8549 (1990)
10.19 K. Kern, U. Becher, P. Zeppenfeld, B. Hall, D.L. Mills: Chem. Phys. Lett. **167**, 362 (1990)
10.20 B. Poelsema, S.T. de Zwart, G. Comsa: Phys. Rev. Lett. **49**, 578 (1982); (E) **51**, 522 (1983).
10.21 F.C. Frank, J.H. van der Merwe: Proc. Roy. Soc. A **198**, 216 (1949)
10.22 P. Bak, D. Mukamel, J. Villain, K. Wentowska: Phys. Rev. B **19**, 1610 (1979)
10.23 E.D. Specht, A. Mak, C. Peters, M. Sutton, R.J. Birgeneau, K.L. D'Amico, D.E. Moncton, S.E. Nagler, P.M. Horn: Z. Phys. B **69**, 347 (1987); S.C. Fain, M.D. Chinn, R.D. Diehl: Phys. Rev. B **21**, 4170 (1980)
10.24 K. Kern, R. David, P. Zeppenfeld, R.L. Palmer, G. Comsa: Solid State Commun. **62**, 361 (1987)
10.25 M.B. Gordon, J. Villain: J. Phys. C **18**, 391 (1985)

10.26 V.L. Pokrovsky, A.L. Talapov: Sov. Phys. JETP **51**, 134 (1980)
10.27 K. Kern: Phys. Rev. B **35**, 8265 (1987)
10.28 G. Vidali, M.W. Cole: Phys. Rev. B **29**, 6736 (1984)
10.29 P. Bak: Rep. Prog. Phys. **45**, 587 (1982)
10.30 K. Kern, P. Zeppenfeld, R. David, G. Comsa: Phys. Rev. Lett. **59**, 79 (1987)
10.31 J. Villain: J. Phys. (Paris) Lett. **43**, 1551 (1982); M. Kardar, D.R. Nelson: Phys. Rev. Lett. **55**, 1157 (1985)
10.32 K. Kern, P. Zeppenfeld, R. David, G. Comsa: Phys. Rev. Lett. **57**, 3187 (1986)
10.33 R. Miranda, S. Daiser, K. Wandelt, G. Ertl: Surf. Sci. **131**, 61 (1983)
10.34 B. Poelsema, L.K. Verheij, G. Comsa: Phys. Rev. Lett. **49**, 1731 (1982)